Bayesian analysis of the stochastic gravitational-wave background with alternative polarizations for space-borne detectors

Yu Hu, Pan-Pan Wang, Yu-Jie Tan, and Cheng-Gang Shao*

MOE Key Laboratory of Fundamental Physical Quantities Measurement, Hubei Key Laboratory of Gravitation and Quantum Physics, PGMF, and School of Physics, Huazhong University of Science and Technology, 430074 Wuhan, Hubei, China

(Received 27 October 2022; accepted 4 January 2023; published 20 January 2023)

Future space gravitational-wave detectors will detect gravitational waves with high sensitivity in the mHz frequency band. One possible source is the stochastic gravitational-wave background (SGWB), possibly from astronomy and cosmology. Detecting SGWB could provide an opportunity to directly examine the polarization of gravitational waves. While general relativity predicts only two tensor modes for gravitational-wave polarization, general metric theories of gravity allow up to four additional modes, including two vector and two scalar modes. Observing other polarization modes of gravitational waves would directly indicate that general relativity needs to be modified. However, the application of polarization identification methods developed for ground-borne detectors to space-borne detectors will require improvement. In this paper, we design a new statistic for the characteristics of space-borne detectors and perform Bayesian analysis. We analyze the performance of the new statistics, including the signal-to-noise ratio, ability to identify SGWB, and parameter estimation. The results show that the Bayesian method with new statistics is good enough to meet the needs of space detectors to identify polarized SGWB. In particular, space-borne gravitational-wave detectors will have the ability to distinguish the scalar-breathing mode and the scalar-longitudinal mode with this Bayesian method, which ground-based detectors cannot.

DOI: 10.1103/PhysRevD.107.024026

I. INTRODUCTION

Since the first gravitational-wave (GW) signal GW150914 was detected by Advanced LIGO in 2015 [1], Advanced LIGO and, later, Advanced Virgo have detected nearly a hundred GWs sourced from compact binary coalescences [2–6], which open the era of gravitational-wave astronomy. In addition to obtaining astronomical information, GWs provide an opportunity to test gravity in a strong field [7–10]. Among them, the test of gravitational-wave polarization is an important component. General relativity (GR) predicts that there only exist two tensor polarizations for gravitational wave, the plus and cross modes. However, there are four additional polarizations allowed by the generic metric theories of gravity, including two vector modes and two scalar modes [11–15]. If these additional polarizations are detected, it would represent a clear violation of general relativity.

In the recent years, with the successful operation of more and more ground-based detectors, the ground-based detection network has begun to support polarization analysis [16–19]. However, because of the lack of predictions for the template of inspiral-merger-ringdown GW signal in modified gravity, the limit of alternative polarizations through compact binary coalescences signals is still weak. In addition to directly detecting gravitational waves from binary star mergers, another important goal of the detector is to observe the stochastic gravitational-wave background. There are numerous sources of stochastic gravitational-wave background (SGWB), for example, the superposition of a large number of unidentifiable weak binary signals [20–23]. In addition to the astrophysical sources, there are many ways to generate SGWB in the early Universe, such as cosmological phase transitions [24,25], primordial gravitational waves [26,27], cosmic strings [28,29], etc. The detection of the SGWB can provide another test of polarization.

So far, there is no clear evidence that SGWB has been detected. The detectors of different frequency bands give the independent constraints on SGWB. In the nHz band, the common-spectrum features have been found in data accumulated over many years by the Pulsar Timing Array (PTA), but there is no significant evidence of correlations [30–33], which is necessary to claim a detection of SGWB. In the Hz hand, the ground-based laser interferometers give an upper limit of fractional energy density of SGWB $\Omega_{\mathrm{GW}} \leq 5.8 \times 10^{-9}$ [34]. The future space-based interferometers such as LISA [35], TianQin [36], Taiji [37], and DECIGO [38], will be able to detect SGWB with high sensitivity in the mHz band [39–41]. For more detection

*cgshao@hust.edu.cn

strategies and current status reference, review Refs. [42,43]. Once we have detected the SGWB, we need to answer whether there is only tensor polarization or alternative polarizations are included.

If there are multiple detectors, the different correlation channels formed will be able to separate the mixture of polarization [44,45]. This method can separate different polarizations within each frequency bin and does not require a parametrized model of the energy density spectrum of the background. However, this method is not very sensitive, and the characterization of spectrum of different polarizations is unclear. Another more practical approach is the Bayesian method presented in Ref. [46], which has been used to search for SGWB with alternative polarizations in ground-based detector data [47–49]. The Bayesian method requires model assumptions but is more capable and can provide more information from the data.

Future space-based gravitational-wave detectors are expected to detect SGWB; after all, there are abundant potential sources in their sensitive frequency band. For space-based detectors, how to detect SGWB with alternative polarizations needs to be studied. They will be mobile in space, unlike ground-based detectors, which are relatively stationary once deployed. Recently, a cancellation method based on time delay interferometry (TDI) combination has been proposed [50] and constructs a special combination that is insensitive to tensor polarization. We focus on the applicability of traditional methods for ground-based detectors to space-based detectors. In this paper, we apply the Bayesian method in Ref. [46] to space-based detectors and find that corresponding tuning for space-based detectors is required to improve performance. We design a new statistic and analyze the performance of detection and characterization of SGWB with alternative polarizations.

The outline of the paper is as follows. In Sec. II, we review the SGWB in general metric theories of gravity and the detection method. In Sec. III, we design a new statistic of Bayesian analysis for space-borne detectors. Then, we calculate its signal-to-noise ratio (SNR) and evaluate its performance. In Sec. IV, the Bayesian mode selection is used to determine whether the data contain background signal and whether the signal contains alternative polarizations. The odds ratio to identify alternative polarizations is constructed somewhat differently from the previous literature. Then, in Sec. V, the aspect of parameter estimation is discussed, especially for the case involving two scalar polarizations. Finally, a discussion is presented in Sec. VI.

II. DESCRIPTION AND DETECTION OF SGWB

A. Stochastic background with non-GR polarizations

The metric perturbations at any spacetime point $(t,\vec{x})$ corresponding to SGWB can be expressed as a superposition of plane waves of different frequencies from different directions [42],

$$h_{ab}(t,\vec{x}) = \int_{-\infty}^{\infty} df \int d^2\Omega_{\hat{n}} \sum_A h_A(f,\hat{n}) e^A_{ab}(\hat{n}) e^{i2\pi f(t+\hat{n}\cdot\vec{x}/c)}, \tag{1}$$

where $A = \{+,\times,X,Y,B,L\}$ represents different polarization modes, where $+,\times$ represent tensor modes predicted by general relativity and X, Y and B, L represent vector and scalar modes allowed by the general metric theory of gravity. Explicitly, for GW coming from the sky direction $\hat{n}$, the six spin-2 polarization basis tensors are

$$\begin{aligned} e^+_{ab}(\hat{n}) &= \hat{\theta}_a\hat{\theta}_b - \hat{\phi}_a\hat{\phi}_b, & e^\times_{ab}(\hat{n}) &= \hat{\theta}_a\hat{\phi}_b + \hat{\phi}_a\hat{\theta}_b, \\ e^X_{ab}(\hat{n}) &= \hat{\theta}_a\hat{n}_b + \hat{n}_a\hat{\theta}_b, & e^Y_{ab}(\hat{n}) &= \hat{\phi}_a\hat{n}_b + \hat{n}_a\hat{\phi}_b, \\ e^B_{ab}(\hat{n}) &= \hat{\theta}_a\hat{\theta}_b + \hat{\phi}_a\hat{\phi}_b, & e^L_{ab}(\hat{n}) &= \sqrt{2}\hat{n}_a\hat{n}_b, \end{aligned} \tag{2}$$

where $\hat{\theta}$, $\hat{\phi}$ are perpendicular to the propagation direction:

$$\begin{aligned} \hat{n} &= (\sin\theta\cos\phi, \sin\theta\sin\phi, \cos\theta), \\ \hat{\theta} &= (\cos\theta\cos\phi, \cos\theta\sin\phi, -\sin\theta), \\ \hat{\phi} &= (-\sin\phi, \cos\phi, 0). \end{aligned} \tag{3}$$

The fourier coefficients $h_A(f,\hat{n})$ are random variables, whose statistic is significant. The statistical properties of the SGWB are described by the probability distribution of the metric perturbations. In this work, we assume that the SGWB is Gaussian, stationary, and isotropic. So, only the quadratic expectation is needed to describe its statistical behavior,

$$\langle h_A(f,\hat{n}) h^*_{A'}(f',\hat{n}')\rangle = \frac{1}{8\pi} S^A_h(f)\delta(f-f')\delta_{AA'}\delta^2(\hat{n},\hat{n}'), \tag{4}$$

where $S^A_h(f)$ can be regarded as the component corresponding to the A polarization of a one-sided gravitational-wave strain power spectral density function. Here, the square bracket indicates ensemble average and can be evaluated by doing spatial averages under the assumptions above. We further assume that both the tensor and vector modes are unpolarized, which implies that

$$\begin{aligned} S^+_h &= S^\times_h = S^T_h/2, \\ S^X_h &= S^Y_h = S^V_h/2. \end{aligned} \tag{5}$$

However, the two scalar modes should be considered as two independent polarization modes, since one is the longitudinal and the other is transverse.

Conventionally, SGWB is described by its fractional energy density [51],

$$\Omega_{\rm gw}^{A}(f) = \frac{1}{\rho_c}\frac{d\rho_{\rm gw}^{A}}{d\ln f}, \tag{6}$$

defined as the energy density of the component of A polarization per logarithmic frequency bin $d\ln f$, normalized by the critical energy density of the closed Universe $\rho_c \equiv 3c^2H_0^2/8\pi G$. Here G is the gravitational constant, and $H_0 = 67.4\ \mathrm{km\,s^{-1}\,Mpc^{-1}}$ is the Hubble constant [52]. In general relatively, the relation between $S_h^A(f)$ and $\Omega_{\rm gw}^A(f)$ is [51]

$$\Omega_{\rm gw}^{A}(f) = \frac{2\pi^2}{3H_0^2}f^3 S_h^A(f). \tag{7}$$

Note that Eq. (7) holds only if the stress energy of gravitational waves obeys Isaacson's formula [53]:

$$\rho_{\rm gw} = \frac{c^2}{32\pi G}\langle \dot{h}_{ab}(t,\vec{x})\dot{h}^{ab}(t,\vec{x})\rangle. \tag{8}$$

However, in some alternative theories of gravity, the situation is different, in which case we consider $\Omega_{\rm gw}^A(f)$ as a function of the observable $S_h^A(f)$ rather than the fractional energy density.

B. Correlation analysis

Since SGWB is weak and random, it will be masked by noise and difficult to identify in a single detector. Fortunately, SGWB introduces a correlated signal into multiple detectors. The correlation analysis is a standard method used to detect SGWB [51]. SGWB can be searched by measuring the cross-correlation between two detectors,

$$\hat{C}(f) \propto \tilde{s}_I(f)\tilde{s}_J^*(f), \tag{9}$$

where $\tilde{s}_I(f)$ and $\tilde{s}_J(f)$ are frequency domain data for a pair of detectors. If SGWB is present and the noise of the two detectors is uncorrelated, the expected cross-correlation between two detectors is

$$\begin{aligned}\langle \tilde{s}_I(f)\tilde{s}_J^*(f')\rangle &\approx \langle \tilde{h}_I(f)\tilde{h}_J^*(f')\rangle \\ &= \frac{1}{2}\delta(f-f')\sum_A \Gamma_{IJ}^A(f)S_h^A(f),\end{aligned} \tag{10}$$

where the overlap reduction functions (ORFs) are regarded as the response of the detector pair correlation to the isotropic background of each polarization [44,51],

$$\Gamma_{IJ}^A(f) = \frac{1}{8\pi}\int d^2\Omega_{\hat{n}}\sum_{p\in A} R_I^p(f,\hat{n})R_J^{p*}(f,\hat{n}). \tag{11}$$

Here, $R_I^p(f,\hat{n})$ is the antenna response function of the Ith detector to signals with polarization p.

The prerequisite for correlated data analysis is to calculate the ORFs. However, for the two laser interferometer detectors, it is difficult to obtain analytical results directly from the spatial integration of the product of their response functions. The full expression for the antenna response function of the Michelson-type laser interferometer detector is

$$\begin{aligned}R_I^A(f,\hat{n}) = &\frac{1}{2}e_{ab}^A(\hat{n})[u_I^a u_I^b \mathcal{T}_{\hat{u}_I}(f,\hat{u}_I) - v_I^a v_I^b \mathcal{T}_{\hat{v}_I}(f,\hat{v}_I)] \\ &\times e^{i2\pi f\hat{n}\cdot\vec{r}_I/c},\end{aligned} \tag{12}$$

where $\hat{u}_I$ and $\hat{v}_I$ are the direction vectors of the Ith detector's two arms, respectively, and $\vec{r}_I$ is the position vector. Here,

$$\begin{aligned}&\mathcal{T}_{\hat{u}}(f,\hat{u}) \\ &= \frac{1}{2}e^{-i2\pi fL/c}[e^{-i\pi fL/c(1-\hat{n}\cdot\hat{u})}\mathrm{sinc}(\pi fL/c(1+\hat{n}\cdot\hat{u})) \\ &\quad + e^{i\pi fL/c(1+\hat{n}\cdot\hat{u})}\mathrm{sinc}(\pi fL/c(1-\hat{n}\cdot\hat{u}))]\end{aligned} \tag{13}$$

is the round-trip timing transfer function for photon propagation along $\hat{u}$ with arm length L. For ground-based detectors, the small antenna approximation is accurate enough in the sensitive frequency band. Within the small antenna approximation $2fL/c \ll 1$, the round-trip timing transfer function approximates $\mathcal{T}_{\hat{u}}(f,\hat{u}) \approx 1$, so the response function is reduced to a simple expression, namely,

$$R_I^A(f,\hat{n}) = \frac{1}{2}e_{ab}^A(\hat{n})[u_I^a u_I^b - v_I^a v_I^b]e^{i2\pi f\hat{n}\cdot\vec{r}_I/c}. \tag{14}$$

The analytical expression of ORFs can be obtained within the small antenna approximation [44,51]. It is trivial that the ORF of two detectors dependence on their relative orientation and distance. Surprisingly, there are sufficient constraints for ground-based detectors such that the dependency can be described with only three parameters, one of which is distance and two of which are used to represent relative directions.

The situation is more complicated for space-borne detectors, where the small antenna approximation is not always satisfied within their sensitive frequency bands. The configuration of space-based detectors, with some differences from ground-based detectors, usually consists of three satellites forming six unidirectional laser links. Although it is still possible to form a Michelson interferometer-type channel with four links between the two arms, the instability of the arm length causes the laser phase noise to be too large to achieve gravitational-wave detection. To suppress the laser phase noise, the TDI technology is needed. If the small antenna approximation is applied again, namely, $\mathcal{T}_{\hat{u}}(f,\hat{u}) \approx 1$, the response function of the first-generation TDI Michelson combination X reads

$$R_I^A(f,\hat{n}) = \frac{1}{2}(1 - e^{-i4\pi f L_I/c}) \times e_{ab}^A(\hat{n})[u_I^a u_I^b - v_I^a v_I^b] e^{i2\pi f \hat{n}\cdot\vec{r}_I/c}. \quad (15)$$

Following Ref. [44], the ORFs for different polarizations can be expressed in terms of the detector tensors $D_I^{ab} = 1/2(u_I^a u_I^b - v_I^a v_I^b)$, and the directional vector between two detectors $\hat{s} = \frac{\vec{r}_J - \vec{r}_I}{|\vec{r}_J - \vec{r}_I|}$:

$$\Gamma_{IJ,X}^A(f) = 4e^{i2\pi f(L_J - L_I)/c} \sin(2\pi f L_I/c) \sin(2\pi f L_J/c) \times [\rho_1^A(\alpha) D_I^{ab} D_{J,ab} + \rho_2^A(\alpha) D_I^{ab} D_{J,bc} s_a s^c + \rho_3^A(\alpha) D_I^{ab} D_J^{cd} s_a s_b s_c s_d], \quad (16)$$

where

$$\begin{bmatrix} \rho_1^T \\ \rho_2^T \\ \rho_3^T \end{bmatrix} = \frac{1}{70} \begin{bmatrix} 28 & -40 & 2 \\ 0 & 120 & -20 \\ 0 & 0 & 35 \end{bmatrix} \begin{bmatrix} j_0 \\ j_2 \\ j_4 \end{bmatrix}, \quad (17)$$

$$\begin{bmatrix} \rho_1^V \\ \rho_2^V \\ \rho_3^V \end{bmatrix} = \frac{2}{35} \begin{bmatrix} 7 & 5 & -2 \\ 0 & -15 & 20 \\ 0 & 0 & -35 \end{bmatrix} \begin{bmatrix} j_0 \\ j_2 \\ j_4 \end{bmatrix}, \quad (18)$$

$$2\begin{bmatrix} \rho_1^B \\ \rho_2^B \\ \rho_3^B \end{bmatrix} = \begin{bmatrix} \rho_1^L \\ \rho_2^L \\ \rho_3^L \end{bmatrix} = \frac{2}{105} \begin{bmatrix} 14 & 20 & 6 \\ 0 & -60 & -60 \\ 0 & 0 & 105 \end{bmatrix} \begin{bmatrix} j_0 \\ j_2 \\ j_4 \end{bmatrix}. \quad (19)$$

Here, $j_n(\alpha)$ is the nth-order spherical Bessel function with its variable given by $\alpha(f) = 2\pi f|\vec{r}_J - \vec{r}_I|/c$. Note that the expression of ORFs for the TDI-X channel differs from those of the ground-borne Michelson interferometer in two ways: first, the low-frequency response is remarkably low and proportional to f^2, due to the application of TDI technology, and, second, the phase factor $e^{i2\pi f(L_J - L_I)/c}$ brought about by the difference in arm length makes its imaginary part impossible to ignore. In addition, there is no way to continue simplifying the above expression by choosing the right parameters as for ground-borne detectors. The orientation between two space gravitational-wave detectors is usually not fixed, so the general ORF of space-borne detectors requires six parameters to be fully described, which is much more complex than the three parameters of ground-borne detectors.

The small antenna approximation expression is not accurate enough, and the ORFs of the two scalar polarizations are degenerate. Therefore, we extend the small antenna approximation to develop a more accurate analysis method, consistent with the numerical integration in the sensitive frequency band of the detectors [54]. In addition to the advantage of high precision, our method is not limited to the Michelson-type interferometer but also applies to any TDI combination. Our strategy is to split the integral in ORF for any TDI combination into individual expression between two arms and perform the integration by expanding the expression according to frequency (see Appendix A for details.). The response function of any TDI combination can be expressed as the linear sum of the one-way response of each link multiplied by the delay factor, namely,

$$R_{I,\mathrm{TDI}}^A(f,\hat{n}) = \frac{1}{2} e^{-\frac{i\pi f L}{c}} e_{ab}^A(\hat{n}) \sum_i P_{i,\mathrm{TDI}} u_{I,i}^a u_{I,i}^b \times \mathrm{sinc}\left(\frac{\pi f L}{c}[1 + \hat{n}\cdot\hat{u}_{I,i}]\right) e^{i2\pi f \hat{n}\cdot\vec{r}_{I,i}/c}, \quad (20)$$

where i represents each unidirectional link with a directional vector $\hat{u}_{I,i}$ and the position vector of the midpoint of the link is denoted as $\vec{r}_{I,i}$. Here, $P_{i,\mathrm{TDI}}$ is the delay factor of the TDI combination on the ith link. Thus, the ORFs for any TDI combination can be split into calculations between individual links belonging to two separate detecters, namely,

$$\Gamma_{IJ,\mathrm{TDI}}^A(f) = \frac{1}{8\pi} \int d^2\Omega_{\hat{n}} \sum_{p\in A} R_I^p(f,\hat{n}) R_J^{p^*}(f,\hat{n}) = \frac{e^{\frac{i}{2}(\beta' - \beta)}}{32\pi} \sum_{i,j} P_{I,i} P_{J,j}^* u_i^a u_i^b u_j'^c u_j'^d \times \Gamma_{abcd}^A(\alpha_{ij}, \beta, \beta', \hat{u}_i, \hat{u}_j', \hat{s}_{ij}), \quad (21)$$

where $\beta = 2\pi f L/c, \beta' = 2\pi f L'/c$ (no prime for I detector, with the prime for J detector), and indicators i and j represent a link belonging to detectors I and J, respectively. Only the function Γ_{abcd}^A needs to be evaluated, and the complete expression is

$$\Gamma_{abcd}^A = \int d^2\Omega_{\hat{n}} \,\mathrm{sinc}\left[\frac{\beta}{2}(1 + \hat{n}\cdot\hat{u}_i)\right] \mathrm{sinc}\left[\frac{\beta'}{2}(1 + \hat{n}\cdot\hat{u}_j')\right] \times \sum_{p\in A} e_{ab}^p e_{cd}^p e^{-i\alpha_{ij}\hat{n}\cdot\hat{s}_{ij}}, \quad (22)$$

where $\hat{s}_{ij}$ is the direction vector from the i link of the detector I to the j link of the detector J, and $\alpha_{ij} = 2\pi f \Delta s_{ij}/c$. It is extremely complicated to integrate this expression directly. Given that the low-frequency band contributes most of the SNR, expanding by frequency is a reasonable strategy. Up to the second order of frequency, the expression is approximated as

$$\Gamma_{abcd}^A \approx \int d^2\Omega_{\hat{n}} \left[1 - \frac{\beta^2}{24}(1 + \hat{n}\cdot\hat{u}_i)^2 - \frac{\beta'^2}{24}(1 + \hat{n}\cdot\hat{u}_j')^2\right] \times \sum_{p\in A} e_{ab}^p e_{cd}^p e^{-i\alpha_{ij}\hat{n}\cdot\hat{s}_{ij}}. \quad (23)$$

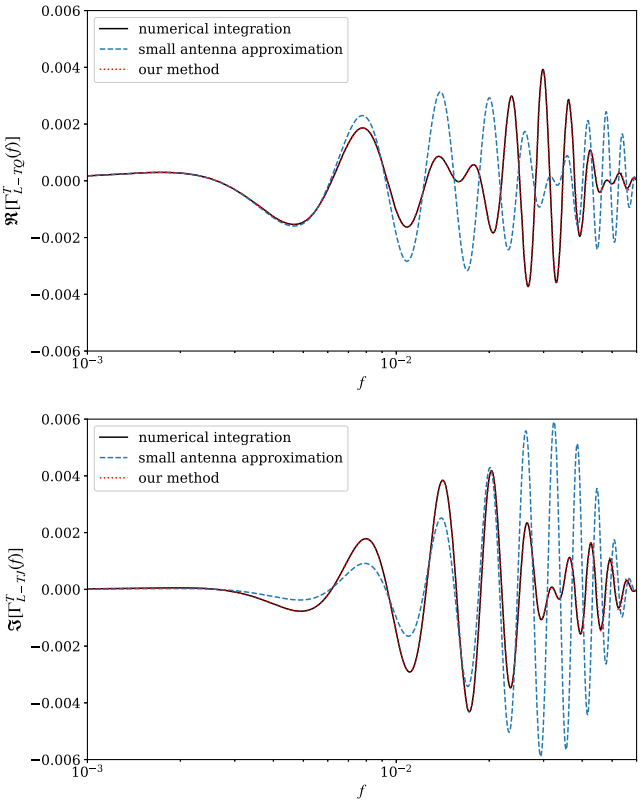

FIG. 1. The comparison of the ORF of LISA-TianQin network for tensor-polarized SGWB calculated by different methods. The above subfigure is the real part of the ORF; the lower one is the imaginary part of the ORF. The ORF of the TDI-X channel at a certain point in the orbit is calculated, adopting numerical integration (black solid), small antenna approximation (blue dashed), and our method (red dotted), respectively.

This expression can be broken down into three parts of computation, where the result of order zero can be found in Ref. [51]. Extending the method proposed in Ref. [51], the other two second-order parts can be analytically calculated. Details and discussion are attached in Appendix A.

Figure 1 displays the tensor ORF of the TDI-X channel for LISA-TianQin network somewhere in the orbit, adopting numerical integration, small antenna approximation, and our method, respectively. Our results are highly consistent with the numerical integration, while the error of the small antenna approximation increases gradually with frequency. In addition, our approach is scalable enough to apply to any TDI channel including combinations that cannot be expressed in Michelson interferometer form because the strategy we employ is to split the calculation of any TDI combination into separate links for operation. What is more, the degeneracy of two scalar polarizations in Eq. (16) is broken. Although the distinction between the ORFs for two scalar polarizations is not particularly obvious, it provides the cornerstone for two scalar polarization resolution.

The orbital characteristics of space-borne detectors make their data analysis somewhat different from those on the ground. While the relative distance and direction of two ground-borne detectors are fixed, the relative orientation of two space detectors may change with the movement. So, the ORF of space-borne detectors may vary with time, while the ground-borne one is constant. The time dependence of space orbit position and direction can be simplified only under the height approximation. Even so, the time dependency after entering the ORFs expression will be too complex. On the other hand, for two space-borne gravitational-wave detectors, an average ORF needs to be defined to characterize the response strength of their cross-correlation signal to SGWB. Take the ORF at N positions in one orbital period of the two detectors and calculate its root mean square, and the desired average ORF is given by

$$\tilde{\Gamma}^A(f) = \sqrt{\frac{1}{N}\sum_{i=1}^{N} |\Gamma_i^A(f)|^2}. \tag{24}$$

We consider three typical space-borne gravitational-wave detector pairs: LISA-TianQin (L-TQ), LISA-Taiji (L-TJ), and TianQin I + II (TQ I + II). The situation of LISA and TianQin is the most complicated. Their sensitive frequency band is different due to the different arm lengths, and the orientation changes are the most complicated because one is the heliocentric orbit and the other is the geocentric orbit. LISA and Taiji are detectors with similar configurations, but at relatively long distances. And the TianQin I + II are similar in configuration, with satellites perpendicular to each other and both orbiting the Earth. The average ORFs for the tensor polarization of these three detector pairs are shown in Fig. 2, in which the TDI-A channel is adopted. The combination of the first-generation TDI Michelson channel can construct noise-orthogonal A and E channels, which are often used when discussing the detection of SGWB. LISA-Taiji has similar and relatively longer arm length, so it is more sensitive in the low-frequency band. On the contrary, the TianQin I + II is more

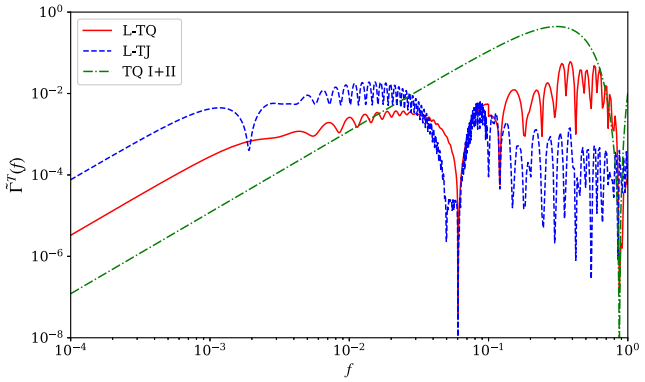

FIG. 2. The average ORF of TDI-A channel for different networks. The red solid line represents the LISA-TianQin network; the blue dashed line represents the LISA-Taiji network; and the green dot-dashed line represents the TQ I-II.

sensitive in the higher-frequency band due to the same and shorter arm length. Moreover, they are all geocentric orbits and are certainly close together, so the upper limit sensitivity is higher than that of LISA-Taiji. Finally, LISA-TianQin falls somewhere in between, as expected. We can conclude that the closer the detectors are, the stronger the detection capability, and the difference in the arm length of the two detectors will lead to a reduction in detection capability.

In addition, ORF changes caused by different orbits can cause other problems. In the next section, we will cover the huge differences in LISA and TianQin orbits, which can cause great trouble with actual data processing for the LISA-TianQin network.

III. STATISTIC OF BAYESIAN ANALYSIS

In actual data analysis, the data are divided into many time segments (labeled by i, $1 \leq i \leq N$). Within each time segment, an estimator is constructed from the cross-correlation of two detectors,

$$\hat{C}_i(f) = \frac{2}{\Delta T}\frac{2\pi^2}{3H_0^2} f^3 \tilde{s}_{1,i}(f)\tilde{s}^*_{2,i}(f), \tag{25}$$

where ΔT is the segment duration that satisfies the requirement to be greater than the light travel time between the two detectors and less than the timescale over which the ORF will vary. The normalization is chosen such that the mean and variance of the estimator are

$$\langle \hat{C}_i(f) \rangle = \sum_A \Gamma_i^A(f)\Omega^A(f) \tag{26}$$

and

$$\sigma_i^2(f) = \frac{1}{2\Delta T \Delta f}\left(\frac{2\pi^2}{3H_0^2}\right)^2 f^6 P_{I,i}(f)P_{J,i}(f), \tag{27}$$

respectively. Here, $\Gamma_i^A(f)$ is the ORF of two detectors for the ith segment, Δf is the frequency bin width, and $P_{I,i}(f)$ and $P_{J,i}(f)$ are the noise power spectral densities of the two detectors. The likelihood function for the N estimators is

$$\mathcal{L}[\hat{C}_i(f)|\mathcal{A}] \propto \exp\left[-\sum_{i=1}^{N}\sum_f \frac{|\hat{C}_i(f) - \sum_A \Gamma_i^A(f)\Omega^A(f)|^2}{2\sigma_i^2(f)}\right], \tag{28}$$

where $\mathcal{A}$ represents a hypothesis that predicts that the background has a specific energy spectrum.

For ground-based detectors, an optimal estimator can be constructed to simplify the Bayesian analysis. The key point is that the ORFs of the two ground-based detectors are invariant once deployed. The analysis of N independent repeated measures is equivalent to that of its average. So, the single cross-power estimator can be constructed as

$$\hat{C}(f) = \frac{\sum_i \hat{C}_i(f)\sigma_i^{-2}(f)}{\sum_i \sigma_i^{-2}(f)}, \tag{29}$$

with the corresponding variance

$$\sigma^{-2}(f) = \sum_i \sigma_i^{-2}(f). \tag{30}$$

And the corresponding likelihood function reduces to

$$\mathcal{L}[\hat{C}(f)|\mathcal{A}] \propto \exp\left[-\sum_f \frac{|\hat{C}(f) - \sum_A \Gamma^A(f)\Omega^A(f)|^2}{2\sigma^2(f)}\right]. \tag{31}$$

The above estimator greatly reduces the computational cost, but when applied to the space-based detectors, it will run into trouble. The problem arises from the fact that the ORFs of two space-based detectors may vary as they orbit to different positions, which means that $\Gamma_i^A(f) \neq \Gamma_j^A(f)$ for $i \neq j$. In this case, the mean of estimator $\hat{C}(f)$ becomes

$$\langle \hat{C}(f) \rangle = \sum_A \bar{\Gamma}^A(f)\Omega^A(f), \tag{32}$$

where $\bar{\Gamma}^A(f) = \frac{1}{N}\sum_{i=1}^{N}\Gamma_i^A(f)$. And $\Gamma^A(f)$ in Eq. (31) will be replaced by $\bar{\Gamma}^A(f)$. The optimal SNR for this estimator is [51]

$$\overline{\mathrm{SNR}}_{\mathrm{opt}} \approx \frac{3H_0^2}{2\pi^2}\sqrt{T}\left[\int_{-\infty}^{\infty} df \frac{|\sum_A \bar{\Gamma}^A(f)\Omega^A(f)|^2}{f^6 P_I(f)P_J(f)}\right]^{1/2}, \tag{33}$$

which is likely to be much smaller than that for individual analysis of the N statistics and then accumulating,

$$\widetilde{\mathrm{SNR}}_{\mathrm{opt}} \approx \frac{3H_0^2}{2\pi^2}\sqrt{T}\left[\int_{-\infty}^{\infty} df \frac{|\sum_A \tilde{\Gamma}^A(f)\Omega^A(f)|^2}{f^6 P_I(f)P_J(f)}\right]^{1/2}. \tag{34}$$

Direct averaging of ORFs at different locations may degrade the SNR, in other words, $|\bar{\Gamma}^A(f)| < |\tilde{\Gamma}^A(f)|$. The ratio of these two averages $|\bar{\Gamma}^A(f)|/|\tilde{\Gamma}^A(f)|$ for different detector pairs and different polarization modes is shown in Fig. 3. The case for the LISA-TianQin is the worst, with the SNR being depressed by orders of magnitude. If no measures are taken, it will be difficult to extract effective information from the data.

Furthermore, the direct mean and root mean square of the ORFs for the LISA-TianQin one-year orbits are shown in Fig. 4. For the LISA-TianQin network, the mean ORF is 2 orders of magnitude smaller than the root-mean-square ORF. Therefore, data analysis with statistic $\hat{C}(f)$ may miss an otherwise strong background signal. It is worth noting that all space gravitational-wave detectors may face such a

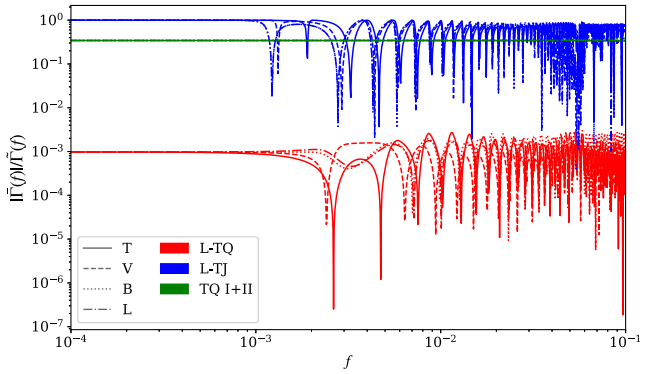

FIG. 3. The ratio of arithmetic mean and root mean square of ORF of TDI-A channel for different networks. Different networks are represented by different colors: LISA-TianQin (red), LISA-Taiji (blue), and TQ I-II (green). And the polarizations are distinguished by line type: tensor (solid), vector (dashed), scalar-breaking (dotted), and scalar-longitudinal (dot-dashed).

problem, since they are relatively moving. The difference is the magnitude of the effect. If the relative distance and orientation of the two detectors are basically unchanged during the orbit, such as LISA-Taiji, the change of ORF are small, and the attenuation of direct average is small as seen in Fig. 3. Below, we will propose a general solution and use LISA-TianQin as an example to demonstrate the practical effect of the above problem.

To avoid the attenuation caused by orbit averaging, we construct estimators for each segment as

$$\hat{C}_i^A(f) = \frac{2}{\Delta T}\frac{2\pi^2}{3H_0^2} f^3 \tilde{s}_{1,i}(f)\tilde{s}^*_{2,i}(f)\Gamma_i^{A^*}(f), \tag{35}$$

and the mean and variance are

$$\langle \hat{C}_i^A(f)\rangle = \Gamma_i^{A^*}(f)\sum_{A'}\Gamma_i^{A'}(f)\Omega^{A'}(f) \tag{36}$$

and

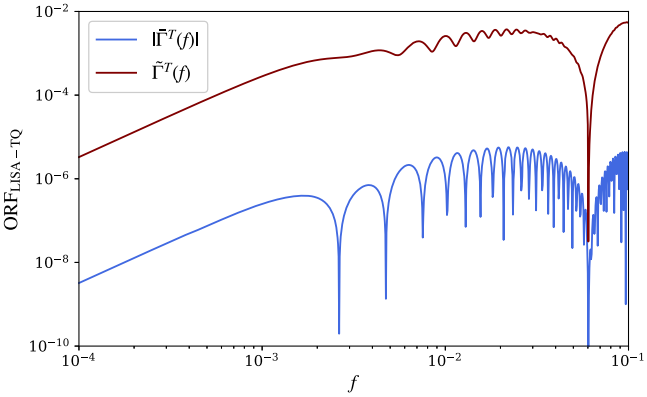

FIG. 4. The mean and root mean square of the ORFs for the LISA-TianQin.

$$(\sigma_i^A(f))^2 = \sigma_i^2(f)|\Gamma_i^A(f)|^2, \tag{37}$$

respectively. The combined single estimator is given by

$$\hat{C}^A(f) = \frac{\sum_i \hat{C}_i^A(f)\sigma_i^{-2}(f)}{\sum_i \sigma_i^{-2}(f)}. \tag{38}$$

The mean and variance are

$$\langle \hat{C}^A(f)\rangle = \sum_{A'} H^{AA'}(f)\Omega^{A'}(f) \tag{39}$$

and

$$(\sigma^A(f))^2 = H^{AA}\sigma^2(f), \tag{40}$$

where $H^{AA'}(f) = \frac{1}{N}\sum_i \Gamma_i^{A*}(f)\Gamma_i^{A'}(f)$. So, the corresponding likelihood function of $\hat{C}^A(f)$ is

$$\mathcal{L}[\hat{C}^A(f)|\mathcal{A}] \propto \exp\left[-\sum_f \frac{|\hat{C}^A(f) - \sum_{A'} H^{AA'}(f)\Omega^{A'}(f)|^2}{2H^{AA}\sigma^2(f)}\right]. \tag{41}$$

The total likelihood function becomes

$$\mathcal{L}[\{\hat{C}^A(f)\}|\mathcal{A}] \propto \prod_A \mathcal{L}[\hat{C}^A(f)|\mathcal{A}]. \tag{42}$$

To assess the power of a statistic, its optimal SNR is required. In the usual way [51], the optimal SNR for statistic $C^A(f)$ is

$$\mathrm{SNR}^A_{\mathrm{opt}} \approx \frac{3H_0^2}{2\pi^2}\sqrt{T}\left[\int_{-\infty}^{\infty} df \frac{|\sum_{A'} H^{AA'}(f)\Omega^{A'}(f)|^2}{f^6 H^{AA}(f)P_I(f)P_J(f)}\right]^{1/2}. \tag{43}$$

Table I lists the SNRs of all four statistics for different purely single polarized SGWB. For SGWB with only a single polarization, $\mathrm{SNR}^A_{\mathrm{opt}}$ for SGWB with A polarization

TABLE I. Optimal SNRs of different statistics $\hat{C}^A(f)$ for different purely tensor, vector, scalar-breathing, and scalar-longitudinal polarized SGWBs. The energy spectrum of SGWB with different polarization are assumed to be power-law distributions with index 2/3, and their amplitudes are chosen such that the optimal SNR calculated by Eq. (34) is 10.

	Tensor	Vector	Breathing	Longitudinal
$\mathrm{SNR}^T_{\mathrm{opt}}$	10.00	6.14	6.03	6.04
$\mathrm{SNR}^V_{\mathrm{opt}}$	4.53	10.00	5.62	5.65
$\mathrm{SNR}^B_{\mathrm{opt}}$	4.84	5.20	10.00	9.93
$\mathrm{SNR}^L_{\mathrm{opt}}$	4.80	5.24	9.93	10.00

TABLE II. Optimal SNRs of different statistics for SGWB with mixed tensor and vector polarizations.

$\widetilde{\mathrm{SNR}}_{\mathrm{opt}}$	$\mathrm{SNR}^{T}_{\mathrm{opt}}$	$\mathrm{SNR}^{V}_{\mathrm{opt}}$	$\mathrm{SNR}^{B}_{\mathrm{opt}}$	$\mathrm{SNR}^{L}_{\mathrm{opt}}$
14.87	11.93	9.22	12.59	12.50

is the same as $\widetilde{\mathrm{SNR}}_{\mathrm{opt}}$. The SNR of the other three statistics not corresponding to A polarization will be reduced, but will still be larger than that of statistic $\hat{C}(f)$. Note that the behaviors of ORFs for two scalar polarizations are similar, so the results of statistics $\hat{C}^B$ and $\hat{C}^L$ are close. For SGWB with mixed polarizations, the SNR of any of the four statistics cannot achieve the optimal SNR. For example, for SGWB with mixed tensor and vector polarization, the SNRs for different statistics are listed in Table II. The spectra of SGWB are chosen as $\Omega^T(f) = 8.59 \times 10^{-12}(f/1\ \mathrm{mHz})^{2/3}$ and $\Omega^V(f) = 7.58 \times 10^{-12}(f/1\ \mathrm{mHz})^{2/3}$, with optimal SNR $\widetilde{\mathrm{SNR}}_{\mathrm{opt}} = 14.87$. The SNR for each statistic $\hat{C}^A(f)$ is slightly smaller than the optimal SNR, but much better than that of the original statistic $\hat{C}(f)$, which is $\overline{\mathrm{SNR}}_{\mathrm{opt}} = 0.01$. We can conclude that $\overline{\mathrm{SNR}}_{\mathrm{opt}} \ll \mathrm{SNR}^{A}_{\mathrm{opt}} \leq \widetilde{\mathrm{SNR}}_{\mathrm{opt}}$ for the LISA-TianQin network. To more directly understand the effect of orbital averaging, we simulate a background of a mixture of tensor and vector polarizations into the data to generate the statistic $\hat{C}_i(f)$. The two individual statistics $\hat{C}(f)$ and $\hat{C}^T(f)$ constructed in different ways are shown in Fig. 5. We can see that it is difficult to distinguish the background signal in the data by $\hat{C}(f)$, although the optimal SNR of the data is high enough.

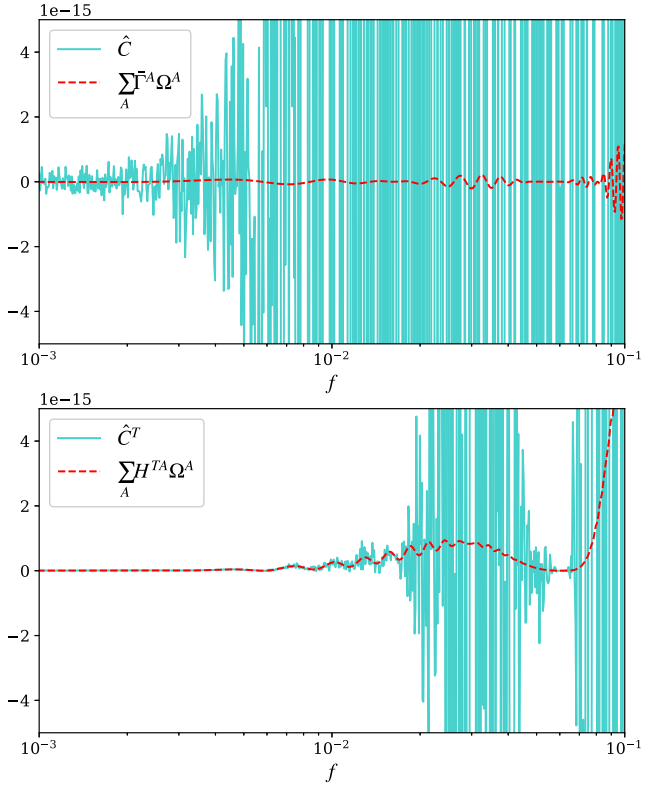

FIG. 5. The simulated measurements $\hat{C}(f)$ (upper) and $\hat{C}^T(f)$ (lower) for a background with mixture of tensor and vector polarizations, recovered after one year of observation with LISA-TianQin network. The parameters of spectra of background for the simulation are $\Omega^T(f) = 8.59 \times 10^{-12}(f/1\ \mathrm{mHz})^{2/3}$ and $\Omega^V(f) = 7.58 \times 10^{-12}(f/1\ \mathrm{mHz})^{2/3}$, with optimal SNR $\widetilde{\mathrm{SNR}}_{\mathrm{opt}} = 14.87$.

IV. DETECTION OF POLARIZED BACKGROUND

General alternative theories of gravity predict that gravitational waves contain a mixture of tensor and other polarizations instead of pure tensor polarization. Even if the alternative polarizations are not concerned, when the background is assumed *a priori* to be pure tensor polarization, any other polarization will interfere with the search for the gravitational-wave background. It is therefore important how to determine whether the data contain a background signal and, if so, whether it contains alternative polarizations which are not allowed by GR. We choose to adopt the Bayesian method proposed in Ref. [46] to detect the gravitational background and identify the alternative polarizations. The detection part is done by Bayesian model selection. After determining whether a signal exists in the data, Bayesian statistics can be employed to obtain a posterior probability density function of the spectral parameters. The PyMultiNest package [55] is used to perform the calculation.

Once the measurement data are given, we can compute Bayesian evidence for various hypotheses to determine whether the data contain a background signal and whether alternative polarizations are present in the signal. We consider three hypotheses:

(1) Gaussian noise (N).—No background signal in the data, and the data consists of Gaussian distributed noise.
(2) Signal (SIG).—The data contain Gaussian distributed noise and signals with any polarization(s) and the assumed spectrum.
(3) Pure tensor-polarized signal (GR).—The data contain Gaussian distributed noise and signals with pure tensor polarization, consistent with GR predictions.

The Bayesian evidence of statistic $\hat{C}^A$ for hypotheses $\mathcal{A}$ with parameters θ_A is defined as

$$P(\hat{C}^A|\mathcal{A}) = \int \mathcal{L}(\hat{C}^A|\theta_A, \mathcal{A})\pi(\theta_A|\mathcal{A})d\theta_A, \qquad (44)$$

where the likelihood $\mathcal{L}(\hat{C}^A|\theta_A, \mathcal{A})$ is given by Eq. (42) and $\pi(\theta_A|\mathcal{A})$ is the prior probability under hypotheses $\mathcal{A}$. The

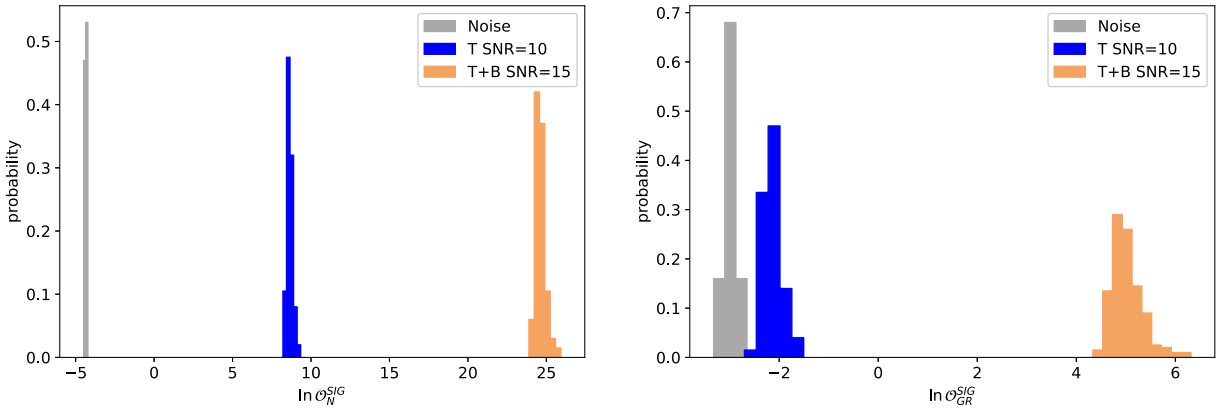

FIG. 6. The distribution of odds ratios $\mathcal{O}_N^{\rm SIG}$ (left) and $\mathcal{O}_{\rm GR}^{\rm SIG}$ (right) for different simulated data. For the Gaussian noise (gray), the distribution of $\mathcal{O}_N^{\rm SIG}$ and $\mathcal{O}_{\rm GR}^{\rm SIG}$ is concentrated and less than 0. And for the pure tensor polarized signal with index $2/3$ (blue), the amplitude is set reasonably so that the SNR is 10. Finally, for a background with mixture of tensor and scalar-breathing polarization (light brown), the indices for two polarizations are both $2/3$, and the amplitude of each polarization component is set reasonably so that the SNR of the individual components is 10 and the total SNR is 15.

energy density spectrum for different hypotheses can be expressed as

$$\begin{aligned}\Omega_N(f) &= 0,\\ \Omega_{\rm GR}(f) &= \Omega_0^T\left(\frac{f}{f_0}\right)^{\alpha_T},\\ \Omega_{\rm SIG}(f) &= \sum_A \Omega_0^A\left(\frac{f}{f_0}\right)^{\alpha_A}.\end{aligned} \tag{45}$$

To meet the needs of data analysis, we can define two odds ratios,

$$\begin{aligned}\mathcal{O}_N^{\rm SIG} &= \frac{P(\hat{C}^A|{\rm SIG})}{P(\hat{C}^A|N)}\frac{\pi({\rm SIG})}{\pi(N)},\\ \mathcal{O}_{\rm GR}^{\rm SIG} &= \frac{P(\hat{C}^A|{\rm SIG})}{P(\hat{C}^A|{\rm GR})}\frac{\pi({\rm SIG})}{\pi({\rm GR})},\end{aligned} \tag{46}$$

where $\pi({\rm SIG})$, $\pi(N)$, and $\pi({\rm GR})$ are the prior probabilities assigned to each hypothesis, and we set them all to 1 in this paper. The former odds ratio $\mathcal{O}_N^{SIG}$ is conventionally defined, which quantities the probability of the presence of a background signal in the data. The latter odds ratio $\mathcal{O}_{\rm GR}^{\rm SIG}$ is somewhat different from that in the literature, which usually defines $\mathcal{O}_{\rm GR}^{\rm NGR}$. The hypothesis NGR is that there is a signal in the data and the signal contains alternative polarizations. It consists of several subsets: a mix of tensor and vector (TV), a mix of tensor and scalar-breathing (TB), and so on. However, it is hard to represent each of its subsets. For example, the hypothesis TV cannot be directly represented as $\Omega_{\rm TV}(f) = \Omega_0^T(\frac{f}{f_0})^{\alpha_T} + \Omega_0^V(\frac{f}{f_0})^{\alpha_V}$, and the restriction $\Omega_0^T, \Omega_0^V \neq 0$ must be added. Otherwise, it will represent the union of the three hypotheses T, V, and TV. Therefore, from this point of view, it is not straightforward to translate the hypothesis NGR into the Bayesian model. Instead, we choose to construct $\mathcal{O}_{\rm GR}^{\rm SIG}$, which has the same effect as $\mathcal{O}_{\rm GR}^{\rm NGR}$. $\mathcal{O}_{\rm GR}^{\rm SIG}$ indicates the possibility that there is a signal in the data but the signal does not agree with the GR prediction.

The distribution of odds ratios $\mathcal{O}_N^{\rm SIG}$ and $\mathcal{O}_{\rm GR}^{\rm SIG}$ gathered from repeated simulations of signals with the same intensity are shown in Fig. 6. The indices are always fixed as $2/3$, and the amplitudes are chosen so that the SNRs of both the tensor and scalar polarization components are 10. For pure tensor and mixed polarization, the specific spectra are $\Omega_T(f) = 8.59\times10^{-12}(f/1\ {\rm mHz})^{2/3}$ and $\{\Omega_T(f) = 8.59\times10^{-12}(f/1\ {\rm mHz})^{2/3}, \Omega_B(f) = 1.71\times 10^{-11}(f/1\ {\rm mHz})^{2/3}\}$. As shown in the left side of Fig. 6, the distribution of $\mathcal{O}_N^{\rm SIG}$ for Gaussian noise is concentrated around $\ln\mathcal{O}_N^{\rm SIG} = -4.3$. In contrast, the pure tensor background yields a distribution around $\ln\mathcal{O}_N^{\rm SIG} = 8.6$ and the mixed polarization background distribution centered at $\ln\mathcal{O}_N^{\rm SIG} = 24.6$. What can be clearly seen in this subfigure is the significant separation in the distribution of these three cases, which means that the existence of a signal in the data and the strength of the signal can be inferred by $\mathcal{O}_N^{\rm SIG}$. The right side of Fig. 6 shows the distribution of $\mathcal{O}_{\rm GR}^{\rm SIG}$, which characterizes the likelihood that alternative polarizations are included in the signal. For Gaussian noise and pure tensor polarized background, $\mathcal{O}_{\rm GR}^{\rm SIG} < 0$. Compared with Gaussian noise, the odd ratios $\mathcal{O}_{\rm GR}^{\rm SIG}$ of pure tensor polarization background are less negative. This is because both the numerator and denominator of odds ratios we construct contain the tensor component. However, it does not affect the determination of whether the signal contains alternative polarizations. The mixed polarized background yields a positive distribution of $\mathcal{O}_{\rm GR}^{\rm SIG}$, centered at $\ln\mathcal{O}_{\rm GR}^{\rm SIG} = 5.1$.

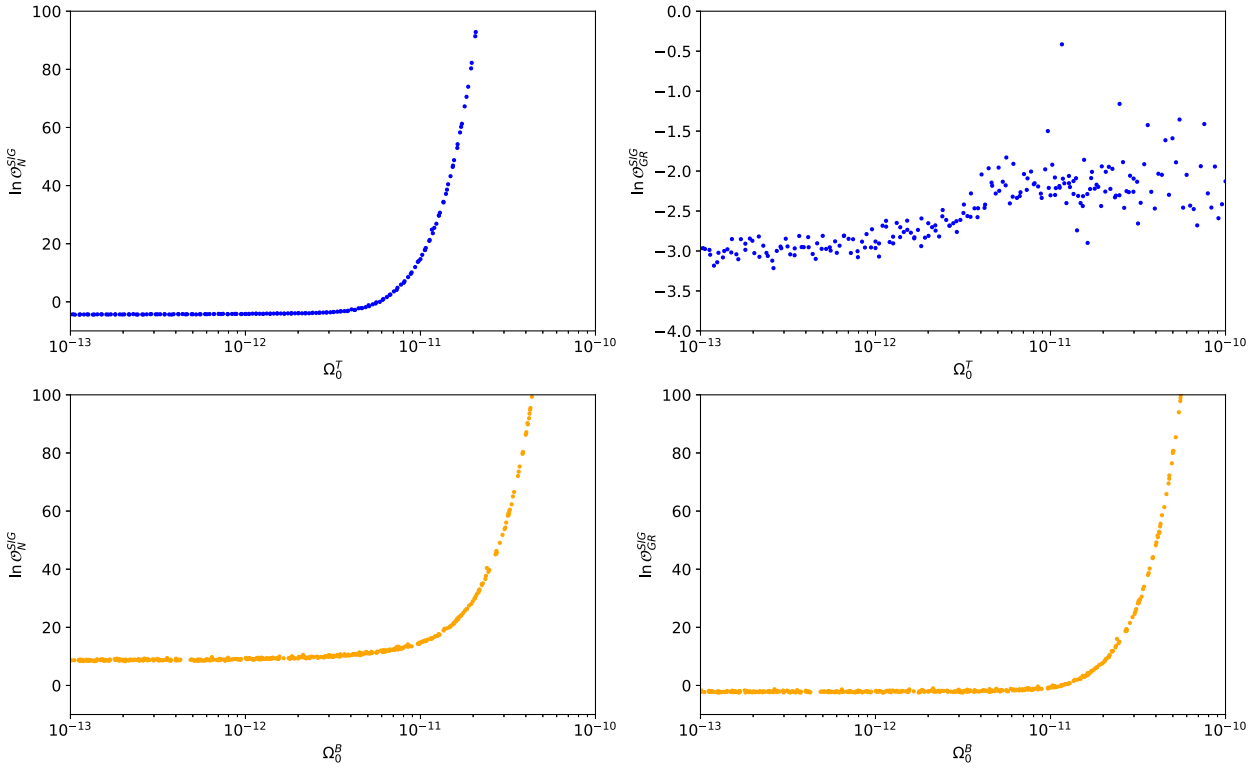

FIG. 7. Odds ratios $\mathcal{O}_N^{\mathrm{SIG}}$ (left) and $\mathcal{O}_{\mathrm{GR}}^{\mathrm{SIG}}$ (right) for different simulated data. Each point in the graph represents a simulation result. The top row is the change in odds ratios as the increase of amplitude for pure tensor background with index $2/3$. The lower row shows the increase in the odds ratio as the amplitude of the scalar-breathing polarization in background increases, mixed with a fixed tensor component.

The variation of odds ratios $\mathcal{O}_N^{\mathrm{SIG}}$ and $\mathcal{O}_{\mathrm{GR}}^{\mathrm{SIG}}$ with amplitudes of background is shown in Fig. 7. For a purely tensor-polarized background, as the amplitude increases, the $\mathcal{O}_N^{\mathrm{SIG}}$ representing the signal strength increases. Naturally, $\mathcal{O}_N^{\mathrm{SIG}}$ depends on the SNR of data, and the specific relationship is $\ln \mathcal{O}_N^{\mathrm{SIG}} \propto \mathrm{SNR}^2$. On the other hand, as the amplitude of pure tensor background increases, $\mathcal{O}_{\mathrm{GR}}^{\mathrm{SIG}}$, which represents the deviation from GR, first increases and then tends to stabilize at -2.2 for loud signal. For the case of remixing the scalar-breathing polarization on the basis of the tensor components, as the amplitude of the scalar-breathing polarization increases, both $\mathcal{O}_N^{\mathrm{SIG}}$ and $\mathcal{O}_{\mathrm{GR}}^{\mathrm{SIG}}$ are

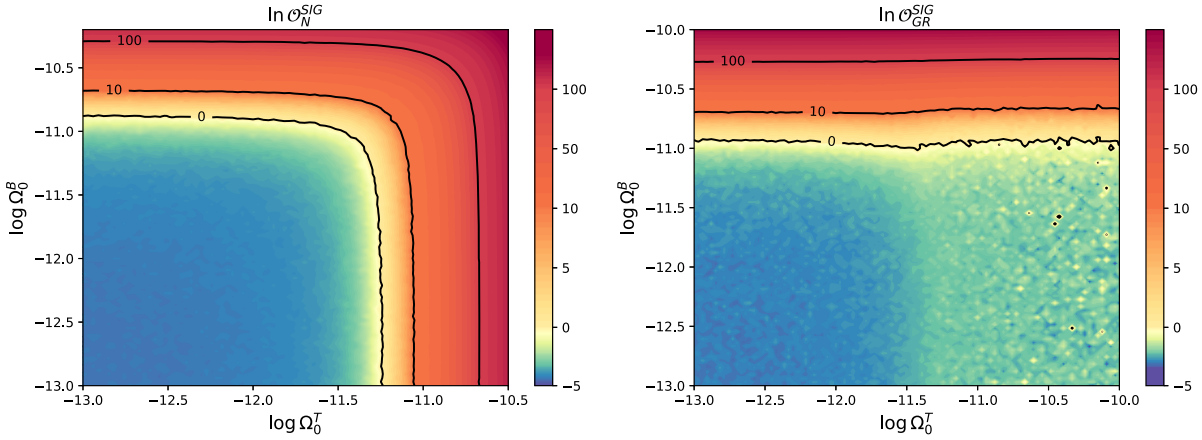

FIG. 8. Odds ratios $\mathcal{O}_N^{\mathrm{SIG}}$ (left) and $\mathcal{O}_{\mathrm{GR}}^{\mathrm{SIG}}$ (right) for simulated data with a background with mixture of tensor and scalar-breathing polarizations. The tensor and scalar-breathing components have the same index $2/3$. The horizontal and vertical coordinates of the left and right images are the same, and they are the amplitudes of the tensor and scalar-breathing components, respectively.

TABLE III. Simulation parameters for each case. The logarithm of the amplitude parameter is in base 10. The odds ratios for each simulation are also shown in the two rightmost columns.

Case	$\log \Omega_0^T$	α_T	$\log \Omega_0^V$	α_V	$\log \Omega_0^B$	α_B	$\log \Omega_0^L$	α_L	$\ln \mathcal{O}_N^{\mathrm{SIG}}$	$\ln \mathcal{O}_{\mathrm{GR}}^{\mathrm{SIG}}$
1. Noise	⋯	⋯	⋯	⋯	⋯	⋯	⋯	⋯	−4.27	−2.86
2. Tensor	−11.07	0.67	⋯	⋯	⋯	⋯	⋯	⋯	9.05	−2.43
3. Tensor + vector	−11.07	0.67	−11.12	0.67	⋯	⋯	⋯	⋯	29.16	1.34
4. Tensor + breathing	−11.07	0.67	⋯	⋯	−10.76	0.67	⋯	⋯	24.60	4.91
5. Tensor + scalar	−11.07	0.67	⋯	⋯	−12.65	3.00	−11.07	0.67	59.64	40.01

expected to continue increasing monotonically. Growth is only apparent once a threshold is exceeded, which means that alternative polarization needs to reach a certain intensity to be recognized.

A more general case is presented in Fig. 8, in which the amplitude of the tensor component is no longer fixed. The left side of Fig. 8 again shows that $\mathcal{O}_N^{\mathrm{SIG}}$ grows with the SNR, regardless of which polarization component contributes. And the right-hand subplot about $\mathcal{O}_N^{\mathrm{SIG}}$ can be roughly divided into three distinct regions. When the amplitude of scalar component is small, $\mathcal{O}_N^{\mathrm{SIG}}$ will increase slightly once the amplitude of the tensor components exceeds a critical value that can be detected. However, its growth is very small, with a small probability of exceeding 0. Only when the amplitude of the alternative polarization component exceeds a certain value, $\mathcal{O}_N^{\mathrm{SIG}}$ will continue to grow with the increase of the amplitude. Whether or not an alternative polarization can be detected depends on its amplitude, independent of the intensity of the tensor component.

V. PARAMETER ESTIMATION OF THE SPECTRUM

After we have determined that the data contain a background signal using Bayesian model selection, the next step is to estimate the parameters of the signal. Alternatively, if there is no signal, an upper limit on the background amplitude for each polarization mode can be placed. Furthermore, we can limit the amplitude of the alternative polarization if it is a background signal that coincides with the GR.

Parameter estimation is performed by using Bayesian statistics to obtain posterior probability density functions (PDFs) for spectral parameters. The PDFs for hypothesis $\mathcal{A}$ are obtained from Bayes's theorem:

$$p(\theta_A|\hat{C}^A,\mathcal{A}) = \frac{p(\hat{C}^A|\theta_A,\mathcal{A})\pi(\theta_A|\mathcal{A})}{P(\hat{C}^A|\mathcal{A})}. \tag{47}$$

The marginalized PDF for a single parameter is obtained by integrating for the rest parameters. The Bayesian upper limit is equivalent to a Bayesian credible interval for a parameter with the lower bound of the interval set to the minimum value that the parameter can take, when the evidence suggests no signal. For example, the 95% credible upper limit $\Omega^{T,95\%}$ on parameter Ω^T is defined by

$$p(\min\Omega^T \le \Omega^T \le \Omega^{T,95\%}|\hat{C}^A,\mathcal{A}) = 0.95, \tag{48}$$

where $\min\Omega^T$ is the minimum value of Ω^T allowed by the prior.

To analyze the ability of Bayesian method to identify polarized background signal, we apply it to simulated data of different situations, including the pure Gaussian noise, a tensor background, and the backgrounds of mixed tensor and other polarizations. The specific simulated parameters for each case and the associated odds ratio are listed in Table III. The odds ratio $\mathcal{O}_N^{\mathrm{SIG}}$ works as expected and can be used to determine whether the data contains background signal. However, the odds ratio $\mathcal{O}_{\mathrm{GR}}^{\mathrm{SIG}}$ performed worse than expected and only worked well if the signal contained a strong alternative polarization. However, the reality is that the alternative polarizations are usually less intense relative to the tensor polarization, if present.

The Bayesian model selection is used to determine whether the data contained background signal and, if so,

TABLE IV. Bayesian estimation of parameters for each case. The top row in each case is the injected parameters, and the bottom row is the Bayesian estimated parameters, or 95% credible upper limits.

Case	$\ln \Omega_0^T$	α_T	$\ln \Omega_0^V$	α_V	$\ln \Omega_0^B$	α_B	$\ln \Omega_0^L$	α_L
1. Noise	< -12.00	⋯	< -12.08	⋯	< -11.71	⋯	< -11.99	⋯
2. Tensor	$-11.10^{+0.13}_{-0.16}$	$0.69^{+0.38}_{-0.41}$	< -11.92	⋯	< -11.58	⋯	< -11.88	⋯
3. Tensor + vector	$-11.02^{+0.18}_{-0.30}$	$0.52^{+0.61}_{-0.46}$	$-11.22^{+0.29}_{-0.50}$	$0.64^{+0.64}_{-0.53}$	< -11.35	⋯	< -11.60	⋯
4. Tensor + breathing	$-11.09^{+0.17}_{-0.24}$	$0.63^{+0.55}_{-0.47}$	< -11.86	⋯	$-11.61^{+0.92}_{-3.12}$	$0.43^{+0.94}_{-2.08}$	$-11.54^{+0.60}_{-3.13}$	$0.41^{+0.82}_{-1.97}$
5. Tensor + scalar	$-10.95^{+0.12}_{-0.25}$	$0.31^{+0.59}_{-0.37}$	< -11.40	⋯	$-12.07^{+0.26}_{-1.21}$	$2.68^{+0.69}_{-0.17}$	$-11.81^{+0.80}_{-3.01}$	$0.42^{+0.96}_{-2.07}$

whether they contained alternative polarizations. At the same time, the posterior PDF of the parameters can be used to estimate the parameters. The PyMultiNest package [55] is used to perform the associated computations. The results are shown in Table IV. First, for the Gaussian noise, there is no evidence that there is a signal, and the 95% credible upper limits on each amplitude are $\log\Omega_0^T < -12.00$, $\log\Omega_0^V < -12.08$, $\log\Omega_0^B < -11.71$, and $\log\Omega_0^L < -11.99$. Second, for the pure tensor background with amplitude $\log\Omega_0^T = -11.07$ and index $\alpha_T = 2/3$, there is strong evidence that there is a background consistent with general relativity, with a central 68% credible interval of $-11.26 < \log\Omega_0^T < -10.97$ and a median value of $\log\Omega_0^T = -11.10$. The 95% credible upper limits on amplitudes of the

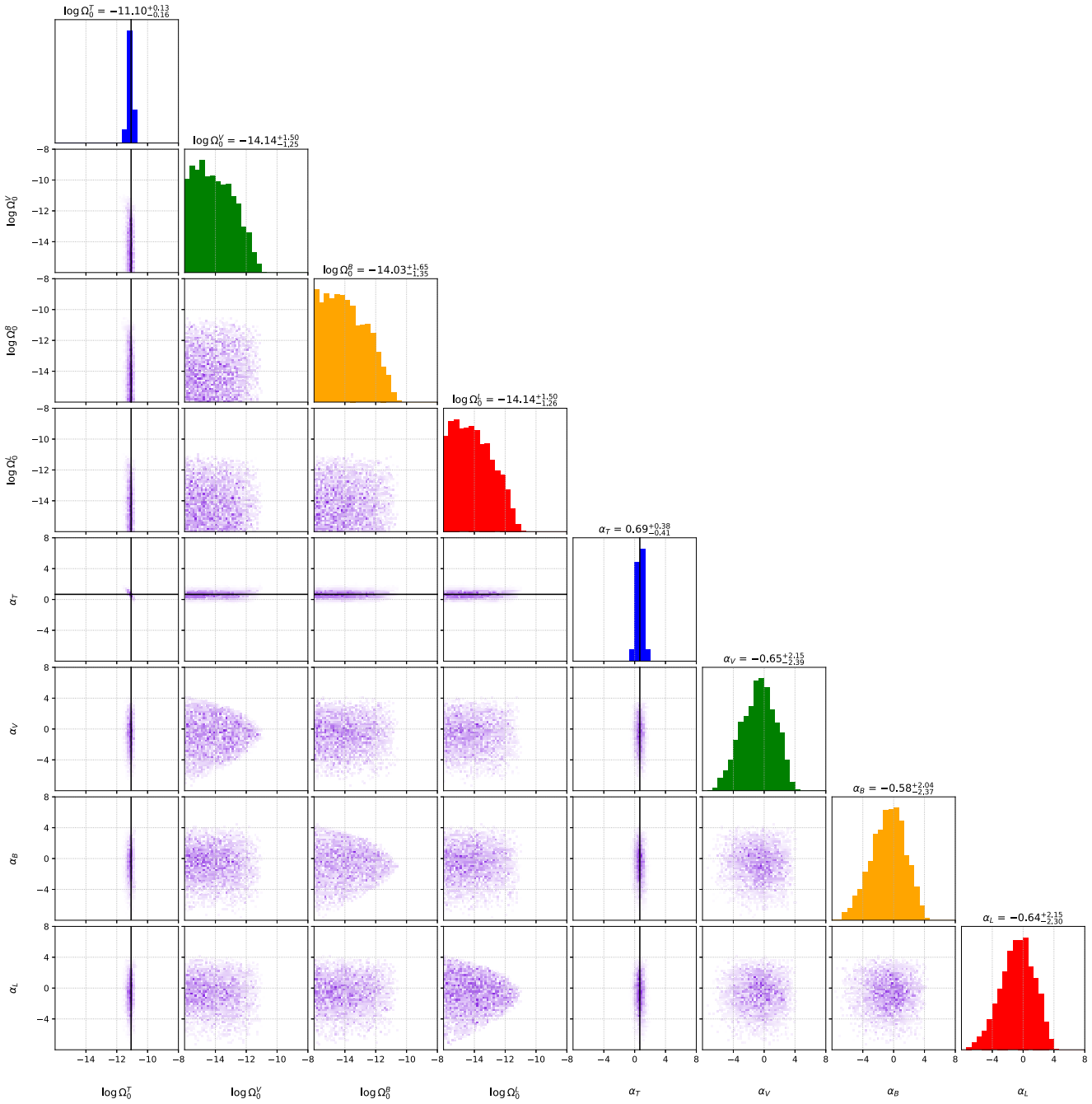

FIG. 9. The posteriors for a simulation of a background with pure tensor polarizations (case 2). The colored histograms along the diagonal show the marginalized one-dimensional posteriors for the amplitudes and slopes of the tensor, vector, scalar-breathingm and scalar-longitudinal polarizations (blue, green, orange, and red, respectively). The rest of the subplots show the joint two-dimensional posteriors between each pair of parameters. The parameters of tensor polarizations are peak around their true values.

alternative polarizations are $\log\Omega_0^V < -11.92$, $\log\Omega_0^B < -11.58$, and $\log\Omega_0^L < -11.88$. The corresponding posteriors are shown in Fig. 9. The colored histograms along the diagonal show the marginalized one-dimensional (1D) posteriors for the amplitudes and slopes of the tensor, vector, scalar-breathing, and scalar-longitudinal polarizations (blue, green, orange, and red, respectively). The rest subplots show the joint two-dimensional (2D) posteriors between each pair of parameters. The real parameters are marked with black lines for comparison. Third, for a background with mixed polarizations of tensor and vector, the two polarization modes can be well resolved as shown in Table IV. And the specific posterior distribution (including the subsequent cases) is shown in Appendix B. However, it is difficult for cases involving scalar polarizations. A single scalar-breathing mode or a single scalar-longitudinal mode is not easily identified accurately but will be identified as a mixture of the two (see case 4). If both modes are included, and the spectral indices of the two differ significantly (e.g., 3 for the breathing mode and $2/3$ for the longitudinal mode in case 5), there is a chance to distinguish the two modes. Or for the case of the same index, the respective signals of the two modes need to be strong enough to be well resolved.

VI. DISCUSSION

In this paper, we studied the data analysis method of alternative polarizations of SGWB with space-borne detectors. Compared with ground-based detectors, the relative motion between different space detectors will affect their correlations. Therefore, the data analysis methods of space-borne detectors to search for the polarized SGWB will be different from those on the ground. We developed a Bayesian method for space-borne gravitational-wave detectors to detect the SGWB with general polarizations or to constrain the amplitudes of alternative polarizations when there is no signal. A new statistic is designed to avoid the decay of SNR for the correlation signal due to average orbital motion. For pure tensors or pure other alternative polarizations, the SNR of the statistic can achieve the optimal SNR.

Taking the LISA-TianQin network as an example, the detection and characterization capabilities of this Bayesian method for SGWB with general polarizations of are analyzed. Because of their orbital differences, orbital averaging can cause significant attenuation of traditional correlation statistics. The new statistic restores signal identifiability. The first step of the specific data analysis is to determine whether the data contain signals. Bayesian model selection is used to do this, and the corresponding odds ratio $\mathcal{O}_N^{\rm SIG}$ is consistent with that in the literature. If the evidence indicates the presence of a signal, another odd ratio $\mathcal{O}_{\rm GR}^{\rm SIG}$ is calculated to determine whether the signal contains alternative polarizations. This odds ratio is constructed differently from $\mathcal{O}_{\rm GR}^{\rm NGR}$ in the literature. It is easier to describe and also has the same ability to identify alternative polarizations. We have performed simulations and show that LISA-TianQin can indeed identify non-tensorial polarizations in SGWB by this method. The next step is to perform parameter estimation of the background signal. The posterior PDFs of the parameters are given by standard Bayesian statistics. Parameter estimation can be used to determine which alternative polarization the signal contains, whether it is a vector, a scalar-breathing mode, a scalar-longitudinal mode, or a mixture of them. If there is no signal, or if the signal is consistent with the GR, the upper limits of the alternate polarizations are given instead.

Interestingly, space-borne detectors have the potential to distinguish between two scalar modes, which ground-borne detectors cannot. In the frequency band where ground detectors are sensitive, the small antenna approximation is fully satisfied, which leads to degeneracy of the response to scalar-breathing and scalar-longitudinal modes. In principle, no matter how advanced data analysis methods are, ground-borne detectors cannot distinguish these two scalar modes of different nature. However, the degeneracy of the responses to the two scalar modes is broken in the relatively high-frequency region where space gravitational-wave detectors are sensitive. This makes it possible to distinguish the two polarizations when the shapes of the spectra for the two scalar modes are very different. Or for the same spectral indices, if the amplitudes of the two modes are large, they can also be distinguished.

ACKNOWLEDGMENTS

We would like to thank Zheng-Cheng Liang and Yi-Ming Hu for helpful discussions. This work is supported by the National Key R&D Program of China under Grant No. 2022YFC2204602, the Natural Science Foundation of China (Grants No. 12247154, No. 11925503), the Postdoctoral Science Foundation of China (Grant No. 2022M711259), Guangdong Major project of Basic and Applied Basic Research (Grant No. 2019B030302001), and the Fundamental Research Funds for the Central Universities, Grant No. HUST: 2172019kfyRCPY029.

APPENDIX A: OVERLAP REDUCTION FUNCTION OF ANY TDI CHANNEL

If a two-detector network is considered as a whole detector, the final output is the cross-correlation of the outputs of the two detectors. Then, the overlap reduction function can be regarded as the response of this whole detector to the gravitational-wave background. It is defined as the sky averaged of the product of the response functions of the two detectors,

$$\Gamma_{IJ}^{A}(f) = \frac{1}{8\pi}\int d^2\Omega_{\hat{n}} \sum_{a\in A} R_I^a(f,\hat{n}) R_J^{a*}(f,\hat{n}), \quad \text{(A1)}$$

where $A = T, V, B, L$. To keep the definitions consistent, the definitions of the two scalars differ by a factor of 2 as

$$\Gamma^B_{IJ}(f) = \frac{1}{4\pi}\int d^2\Omega_{\hat{n}} R^B_I(f,\hat{n}) R^{B*}_J(f,\hat{n}),$$
$$\Gamma^L_{IJ}(f) = \frac{1}{4\pi}\int d^2\Omega_{\hat{n}} R^L_I(f,\hat{n}) R^{L*}_J(f,\hat{n}). \tag{A2}$$

We directly used the original expression without normalizing it, for the convenience of calculation.

In general, the integrals in Eq. (A1) can only be evaluated numerically, due to the complex orientation dependence of the response function. However, for ground-borne interferometers, the integral can be done analytically in the small-antenna limit. In this case, the response function of the Michelson-type interferometer can be expressed as

$$R^a_I(f,\hat{n}) \simeq \frac{1}{2} D^{ab}_I e^a_{ab} e^{i2\pi f \hat{n}\cdot\vec{x}_I/c}, \tag{A3}$$

where D^{ab}_I is the detector tensor defined with the two arm orientation vectors. The expression on the basis of this approximation can be found in Refs. [44,51]. What is more, in the simple case for PTA, the integral can be calculated analytically without any approximation [56].

The situation is a bit more complicated for space-borne interferometers. To suppress the laser phase noise, the TDI technology is applied. Although the Michelson-type interferometer exists among the many TDI combinations, there are many different types of combinations. The response function of those TDI combinations are not as simple as Eq. (A3). The response function of any TDI combination can be expressed as

$$R^A(f,\hat{n}) = \sum_i P_i R^{ab}(f,\hat{n},\hat{u}_i,\vec{r}_i) e^A_{ab}(\hat{n}), \tag{A4}$$

where

$$R^{ab}(f,\hat{n},\hat{u},\vec{r}) = \frac{1}{2} u^a u^b e^{-\frac{i\pi f L}{c}} \sin c\left(\frac{\pi f L}{c}[1+\hat{n}\cdot\hat{u}]\right) \times e^{i2\pi f\hat{n}\cdot\vec{r}/c} \tag{A5}$$

is the response function of a link from one satellite to another, P_i is the delay coefficient of the link, and $\vec{r}$ is the midpoint of the arm. So, the ORF for any TDI channel reads

$$\Gamma^A_{\mathrm{TDI}}(f) = \frac{1}{8\pi}\int d^2\Omega_{\hat{n}} \sum_{p\in A} R^p_I(f,\hat{n}) R^{p^*}_J(f,\hat{n})$$
$$= \frac{e^{\frac{i}{2}(\beta'-\beta)}}{32\pi} \sum_{i,j} P_{I,i} P^*_{J,j} u^a_i u^b_i u'^c_j u'^d_j \times \Gamma^A_{abcd}(\alpha_{ij},\beta,\beta',\hat{u}_i,\hat{u}'_j,\hat{s}_{ij}), \tag{A6}$$

where

$$\Gamma^A_{abcd}(\alpha_{ij},\beta,\beta',\hat{u}_i,\hat{u}'_j,\hat{s}_{ij}) = \int d^2\Omega_{\hat{n}} \sum_{p\in A} \sin c\left(\frac{\beta}{2}[1+\hat{n}\cdot\hat{u}_i]\right) \times \sin c\left(\frac{\beta'}{2}[1+\hat{n}\cdot\hat{u}'_j]\right) e^p_{ab} e^p_{cd} e^{-i\alpha_{ij}\hat{n}\cdot\hat{s}_{ij}}. \tag{A7}$$

Expanding Eq. (A7) by frequency to second order, one obtains that

$$\Gamma^A_{abcd}(\alpha,\beta,\beta',\hat{u},\hat{u}',\hat{s}) = \Gamma^{A(0)}_{abcd}(\alpha,\hat{s}) + \Gamma^{A(2)}_{abcd}(\alpha,\beta,\hat{u},\hat{s}) + \Gamma^{A(2)}_{abcd}(\alpha,\beta',\hat{u}',\hat{s}), \tag{A8}$$

where

$$\Gamma^{A(0)}_{abcd}(\alpha,\hat{s}) = \int d^2\Omega_{\hat{n}} \sum_{p\in A} e^p_{ab} e^p_{cd} e^{-i\alpha\hat{n}\cdot\hat{s}}, \tag{A9}$$

and

$$\Gamma^{A(2)}_{abcd}(\alpha,\beta,\hat{u},\hat{s}) = -\frac{\beta^2}{24}\int d^2\Omega_{\hat{n}} (1+\hat{n}\cdot\hat{u})^2 \sum_{p\in A} e^p_{ab} e^p_{cd} e^{-i\alpha\hat{n}\cdot\hat{s}}. \tag{A10}$$

According to the symmetry of the index, $\Gamma^{A(0)}_{abcd}$ can be constructed as

$$\Gamma^{A(0)}_{abcd}(\alpha,\hat{s}) = A^{A(0)}(\alpha)\delta_{ab}\delta_{cd} + B^{A(0)}(\alpha)(\delta_{ac}\delta_{bd}+\delta_{bc}\delta_{ad}) + C^{A(0)}(\alpha)(\delta_{ab}s_c s_d + \delta_{cd}s_a s_b) + D^{A(0)}(\alpha)(\delta_{ac}s_b s_d + \delta_{ad}s_b s_c + \delta_{bc}s_a s_d + \delta_{bd}s_a s_c) + E^{A(0)}(\alpha)s_a s_b s_c s_d. \tag{A11}$$

The coefficient can be evaluated analytically [44,51]. A system of linear equations for the coefficients $\{A^{A(0)}, B^{A(0)}, \ldots, E^{A(0)}\}$ can be obtained by contracting Eqs. (A9) and (A11) with $\delta_{ab}\delta_{cd}$, $\delta_{ac}\delta_{bd}+\delta_{bc}\delta_{ad}$, $\cdots$, $s_a s_b s_c s_d$. Thus, the expression of the zero order of the ORFs is obtained:

$$\Gamma^{A0}_{IJ,\mathrm{TDI}}(f) = \frac{e^{\frac{i}{2}(\beta'-\beta)}}{32\pi}\sum_{i,j} P_{I,i}P_{J,j}\{A^{A(0)} + 2B^{A(0)}(\hat{u}_i\cdot\hat{u}'_j)^2 + C^{A(0)}((\hat{u}_i\cdot\hat{s}_{ij})^2 + (\hat{u}'_j\cdot\hat{s}_{ij})^2) + 4D^{A(0)}(\hat{u}_i\cdot\hat{u}'_j)(\hat{u}_i\cdot\hat{s}_{ij})(\hat{u}'_j\cdot\hat{s}_{ij}) + E^{A(0)}(\hat{u}_i\cdot\hat{s}_{ij})^2(\hat{u}'_j\cdot\hat{s}_{ij})^2\}. \tag{A12}$$

Following the similar ideas, $\Gamma^{A(2)}_{abcd}$ can be constructed as

$$\begin{aligned}\Gamma^{A(2)}_{abcd}(\alpha,\beta,\hat{u},\hat{s}) = {} & A^{A(2)}\delta_{ab}\delta_{cd} + B^{A(2)}(\delta_{ac}\delta_{bd}+\delta_{bc}\delta_{ad}) + C_1^{A(2)}(\delta_{ab}s_c s_d + \delta_{cd}s_a s_b) \\ & + C_2^{A(2)}(\delta_{ab}u_c u_d + \delta_{cd}u_a u_b) + D_1^{A(2)}(\delta_{ac}s_b s_d + \delta_{ad}s_b s_c + \delta_{bc}s_a s_d + \delta_{bd}s_a s_c) \\ & + D_2^{A(2)}(\delta_{ac}u_b u_d + \delta_{ad}u_b u_c + \delta_{bc}u_a u_d + \delta_{bd}u_a u_c) + E_1^{A(2)}s_a s_b s_c s_d + E_2^{A(2)}u_a u_b u_c u_d \\ & + E_3^{A(2)}(u_a u_b s_c s_d + s_a s_b u_c u_d) + E_4^{A(2)}(u_a u_c s_b s_d + u_a u_d s_b s_c + u_b u_c s_a s_d + u_b u_d s_a s_c).\end{aligned} \tag{A13}$$

The coefficients $\{A^{A(2)}, B^{A(2)}, \ldots, E_4^{A(2)}\}$ can be solved in similar way [54]. Combining Eqs. (A6), (A8), (A11), and (A13), we get the second-order expansion of ORFs, namely,

$$\begin{aligned}\Gamma^{A2}_{IJ}(f) = {} & \frac{e^{\frac{i}{2}(\beta'-\beta)}}{32\pi}\sum_{i,j} P_{I,i}P_{J,j}\{A^{A(0)} + A^{A(2)} + A'^{A(2)} + 2(B^{A(0)} + B^{A(2)} + B'^{A(2)})(\hat{u}_i\cdot\hat{u}'_j)^2 \\ & + (C^{A(0)} + C_1^{A(2)} + C_1'^{A(2)})((\hat{u}_i\cdot\hat{s}_{ij})^2 + (\hat{u}'_j\cdot\hat{s}_{ij})^2) + (C_2^{A(2)} + C_2'^{A(2)})((\hat{u}_i\cdot\hat{u}'_j)^2 + 1) \\ & + 4(D^{A(0)} + D_1^{A(2)} + D_1'^{A(2)})(\hat{u}_i\cdot\hat{u}'_j)(\hat{u}_i\cdot\hat{s}_{ij})(\hat{u}'_j\cdot\hat{s}_{ij}) + 4(D_2^{A(2)} + D_2'^{A(2)})(\hat{u}_i\cdot\hat{u}'_j)^2 \\ & + (E^{A(0)} + E_1^{A(2)} + E_1'^{A(2)})(\hat{u}_i\cdot\hat{s}_{ij})^2(\hat{u}'_j\cdot\hat{s}_{ij})^2 + (E_2^{A(2)} + E_2'^{A(2)})(\hat{u}_i\cdot\hat{u}'_j)^2 \\ & + E_3^{A(2)}((\hat{u}'_j\cdot\hat{s}_{ij})^2 + (\hat{u}_i\cdot\hat{s}_{ij})^2(\hat{u}_i\cdot\hat{u}'_j)^2) + E_3'^{A(2)}((\hat{u}_i\cdot\hat{s}_{ij})^2 + (\hat{u}'_j\cdot\hat{s}_{ij})^2(\hat{u}_i\cdot\hat{u}'_j)^2) \\ & + 4(E_4^{A(2)} + E_4'^{A(2)})(\hat{u}_i\cdot\hat{u}'_j)(\hat{u}_i\cdot\hat{s}_{ij})(\hat{u}'_j\cdot\hat{s}_{ij})\}.\end{aligned} \tag{A14}$$

APPENDIX B: PARAMETER ESTIMATION FOR SGWB WITH MIXED POLARIZATION

In the figures in this Appendix, we show the parametric posterior distribution of the SGWB with mixture of tensor and other polarization.

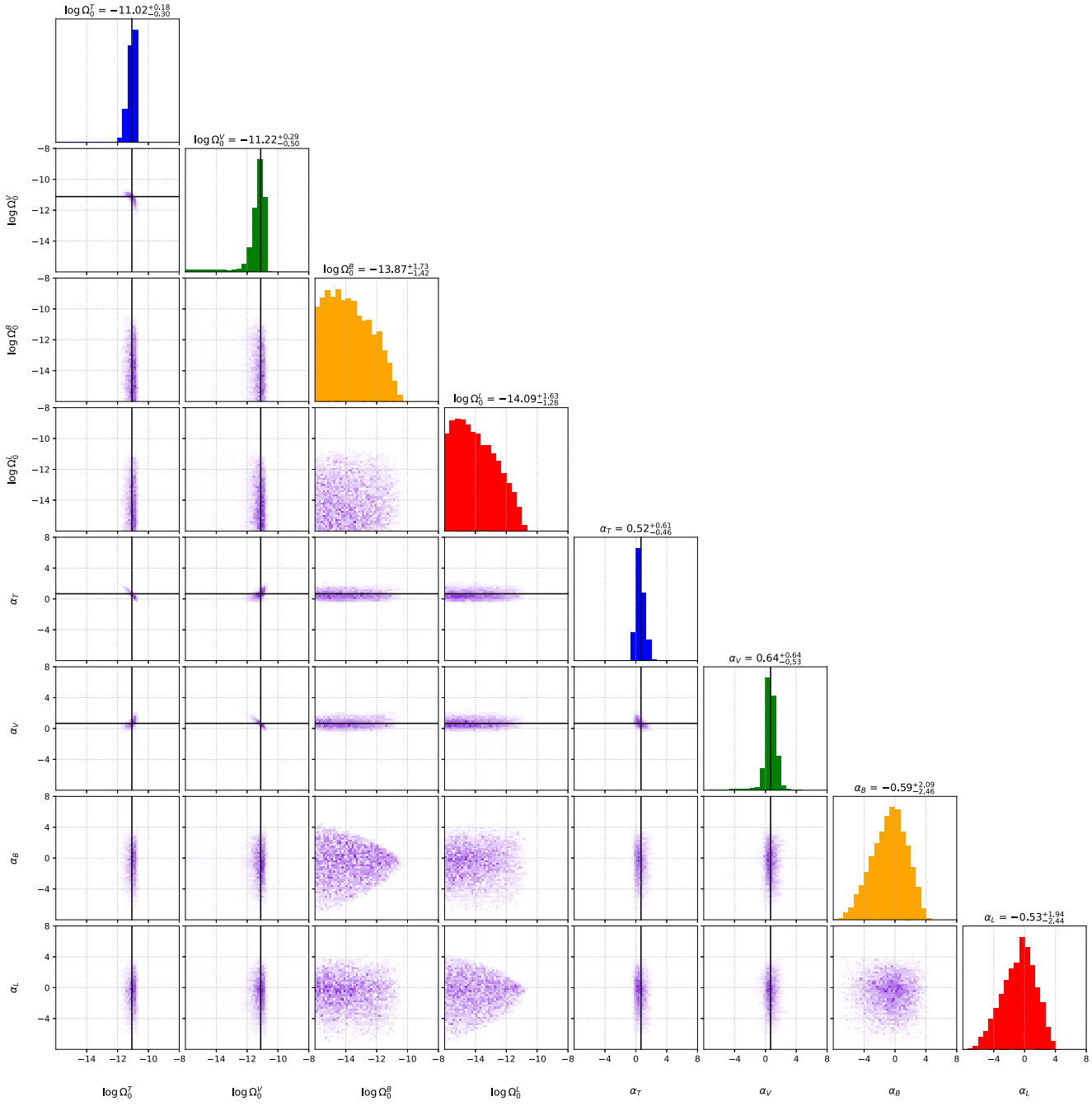

FIG. 10. The posteriors for a simulation of a background with mixed tensor and vector polarizations (case 3). The colored histograms along the diagonal show the marginalized one-dimensional posteriors for the amplitudes and slopes of the tensor, vector, scalar-breathing, and scalar-longitudinal polarizations (blue, green, orange, and red, respectively). The rest of the subplots show the joint two-dimensional posteriors between each pair of parameters. The parameters of tensor and vector polarizations are peak around their true values.

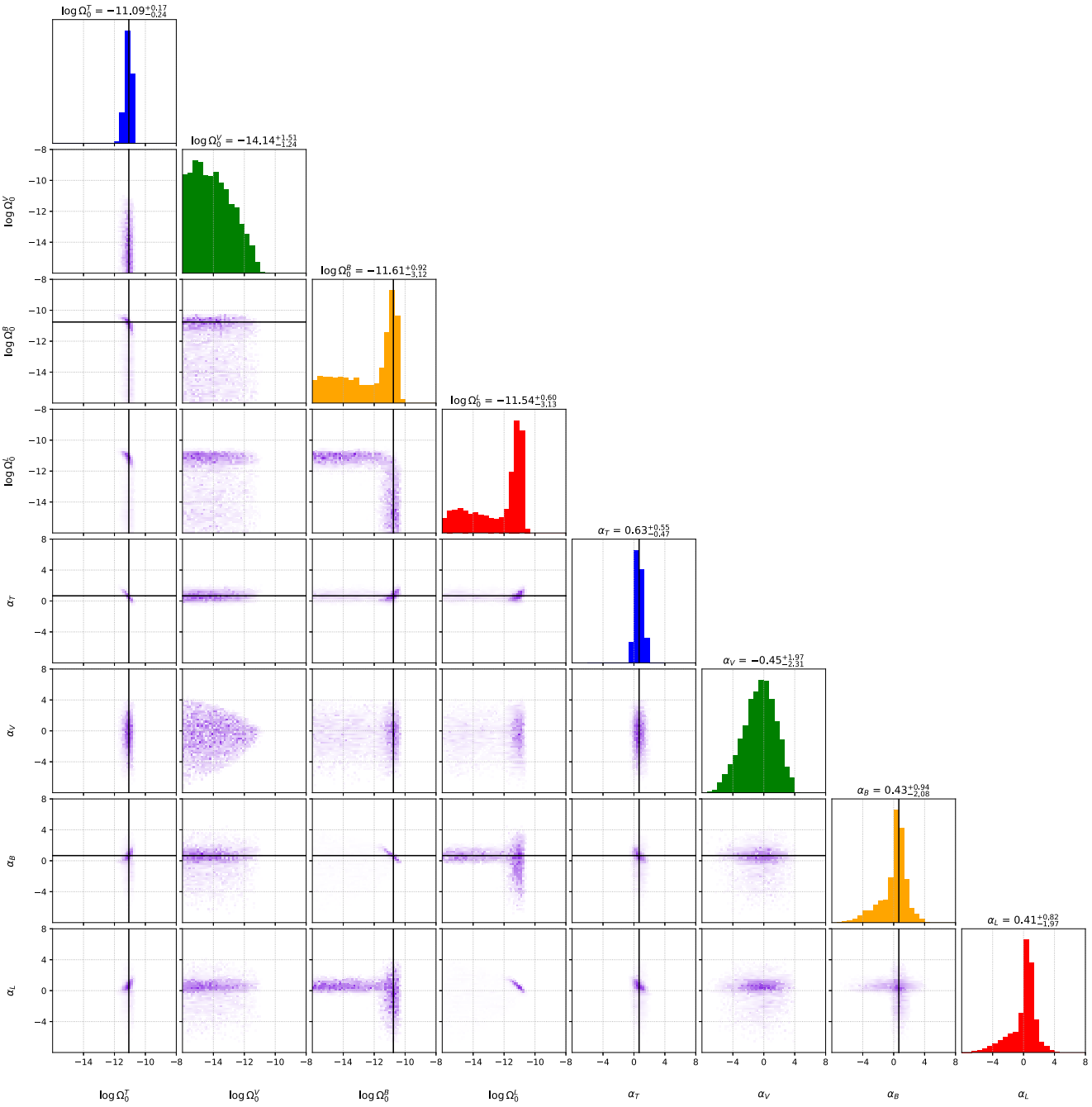

FIG. 11. The posteriors for a simulation of a background with mixed tensor and scalar-breathing polarizations (case 4). The parameters of the tensor polarization agree with the true value within the error range. However, the injected scalar-breathing component was incorrectly identified as a mixture of scalar-breathing and scalar-longitudinal modes.

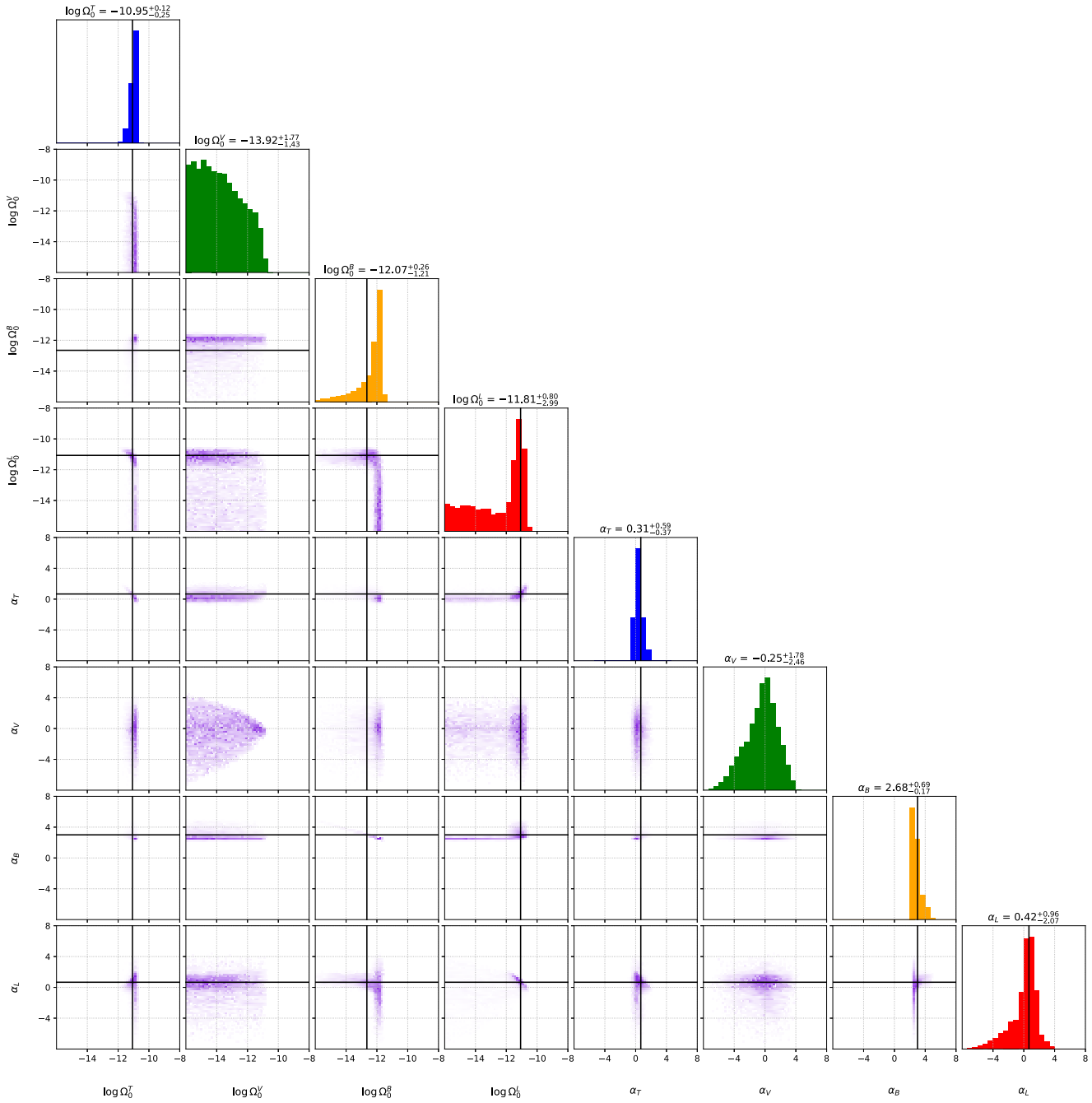

FIG. 12. The posteriors for a simulation of a background with mixed tensor and two scalar polarizations (case 5). The parameters of the tensor and the two scalar polarizations are all consistent with the true values within the error range. This is because the spectra of the two scalars are very different: 3 for the scalar-breathing and 2/3 for the scalar-longitudinal mode.

[1] B. P. Abbott *et al.*, Phys. Rev. Lett. **116**, 061102 (2016).
[2] B. P. Abbott *et al.*, Phys. Rev. Lett. **119**, 161101 (2017).
[3] R. Abbott *et al.*, Astrophys. J. Lett. **915**, L5 (2021).
[4] B. P. Abbott *et al.* (LIGO Scientific and Virgo Collaborations), Phys. Rev. X **6**, 041015 (2016).
[5] B. P. Abbott *et al.* (LIGO Scientific and Virgo Collaborations), Phys. Rev. X **9**, 031040 (2019).

[6] R. Abbott *et al.* (LIGO Scientific and Virgo Collaborations), Phys. Rev. X **11**, 021053 (2021).
[7] C. M. Will, Living Rev. Relativity **17**, 4 (2014).
[8] B. P. Abbott *et al.* (LIGO Scientific and Virgo Collaborations), Phys. Rev. Lett. **116**, 221101 (2016).
[9] C. de Rham, J. T. Deskins, A. J. Tolley, and S.-Y. Zhou, Rev. Mod. Phys. **89**, 025004 (2017).
[10] B. P. Abbott *et al.*, Astrophys. J. Lett. **848**, L13 (2017).
[11] C. Brans and R. H. Dicke, Phys. Rev. **124**, 925 (1961).
[12] D. M. Eardley, D. L. Lee, and A. P. Lightman, Phys. Rev. D **8**, 3308 (1973).
[13] T. Jacobson and D. Mattingly, Phys. Rev. D **70**, 024003 (2004).
[14] E. Sagi, Phys. Rev. D **81**, 064031 (2010).
[15] D. Liang, Y. Gong, S. Hou, and Y. Liu, Phys. Rev. D **95**, 104034 (2017).
[16] B. P. Abbott *et al.* (LIGO Scientific and Virgo Collaborations), Phys. Rev. Lett. **119**, 141101 (2017).
[17] Y. Hagihara, N. Era, D. Iikawa, and H. Asada, Phys. Rev. D **98**, 064035 (2018).
[18] H. Takeda, S. Morisaki, and A. Nishizawa, Phys. Rev. D **103**, 064037 (2021).
[19] R. Abbott *et al.* (LIGO Scientific and Virgo Collaborations), Phys. Rev. D **103**, 122002 (2021).
[20] P. A. Rosado, Phys. Rev. D **84**, 084004 (2011).
[21] X.-J. Zhu, E. Howell, T. Regimbau, D. Blair, and Z.-H. Zhu, Astrophys. J. **739**, 86 (2011).
[22] C. Wu, V. Mandic, and T. Regimbau, Phys. Rev. D **85**, 104024 (2012).
[23] X.-J. Zhu, E. J. Howell, D. G. Blair, and Z.-H. Zhu, Mon. Not. R. Astron. Soc. **431**, 882 (2013).
[24] C. Hogan, Mon. Not. R. Astron. Soc. **218**, 629 (1986).
[25] C. Caprini, R. Durrer, and X. Siemens, Phys. Rev. D **82**, 063511 (2010).
[26] V. Mukhanov, H. Feldman, and R. Brandenberger, Phys. Rep. **215**, 203 (1992).
[27] M. S. Turner, Phys. Rev. D **55**, R435 (1997).
[28] T. Damour and A. Vilenkin, Phys. Rev. D **71**, 063510 (2005).
[29] X. Siemens, V. Mandic, and J. Creighton, Phys. Rev. Lett. **98**, 111101 (2007).
[30] Z. Arzoumanian *et al.*, Astrophys. J. Lett. **905**, L34 (2020).
[31] S. Chen *et al.*, Mon. Not. R. Astron. Soc. **508**, 4970 (2021).
[32] B. Goncharov *et al.*, Astrophys. J. Lett. **917**, L19 (2021).
[33] J. Antoniadis *et al.*, Mon. Not. R. Astron. Soc. **510**, 4873 (2022).
[34] R. Abbott *et al.* (LIGO Scientific, Virgo, and KAGRA Collaborations), Phys. Rev. D **104**, 022004 (2021).
[35] P. Amaro-Seoane *et al.*, arXiv:1702.00786.
[36] J. Luo *et al.*, Classical Quantum Gravity **33**, 035010 (2016).
[37] W.-R. Hu and Y.-L. Wu, Natl. Sci. Rev. **4**, 685 (2017).
[38] S. Kawamura *et al.*, Classical Quantum Gravity **28**, 094011 (2011).
[39] Z.-C. Liang, Y.-M. Hu, Y. Jiang, J. Cheng, J.-d. Zhang, and J. Mei, Phys. Rev. D **105**, 022001 (2022).
[40] G. Wang and W.-B. Han, Phys. Rev. D **104**, 104015 (2021).
[41] N. Seto, Phys. Rev. D **102**, 123547 (2020).
[42] J. D. Romano, and N. J. Cornish, Living Rev. Relativity **20**, 2 (2017).
[43] A. I. Renzini, B. Goncharov, A. C. Jenkins, and P. M. Meyers, Galaxies **10**, 34 (2022).
[44] A. Nishizawa, A. Taruya, K. Hayama, S. Kawamura, and M.-A. Sakagami, Phys. Rev. D **79**, 082002 (2009).
[45] A. Nishizawa, A. Taruya, and S. Kawamura, Phys. Rev. D **81**, 104043 (2010).
[46] T. Callister, A. Sylvia Biscoveanu, N. Christensen, M. Isi, A. Matas, O. Minazzoli, T. Regimbau, M. Sakellariadou, J. Tasson, and E. Thrane, Phys. Rev. X **7**, 041058 (2017).
[47] B. P. Abbott *et al.* (LIGO Scientific and Virgo Collaborations), Phys. Rev. Lett. **120**, 201102 (2018).
[48] B. P. Abbott *et al.* (LIGO Scientific and Virgo Collaborations), Phys. Rev. D **100**, 061101 (2019).
[49] R. Abbott *et al.* (LIGO Scientific, Virgo, and KAGRA Collaborations), Phys. Rev. D **104**, 022004 (2021).
[50] H. Omiya and N. Seto, Phys. Rev. D **102**, 084053 (2020).
[51] B. Allen and J. D. Romano, Phys. Rev. D **59**, 102001 (1999).
[52] Planck Collaboration *et al.*, Astron. Astrophys. **641**, A6 (2020).
[53] R. A. Isaacson, Phys. Rev. **166**, 1272 (1968).
[54] Y. Hu, P.-P. Wang, Y.-J. Tan, and C.-G. Shao, arXiv:2209.07049.
[55] J. Buchner, A. Georgakakis, K. Nandra, L. Hsu, C. Rangel, M. Brightman, A. Merloni, M. Salvato, J. Donley, and D. Kocevski, Astron. Astrophys. **564**, A125 (2014).
[56] Y. Hu, P.-P. Wang, Y.-J. Tan, and C.-G. Shao, Phys. Rev. D **106**, 024005 (2022).